Robotic four-dimensional pixel assembly of van der Waals solids

Andrew J. Mannix [1,9,10], Andrew Ye[2,10], Suk Hyun Sung [3], Ariana Ray[4], Fauzia Mujid[5], Chibeom Park[5], Myungjae Lee[1], Jong-Hoon Kang[5], Robert Shreiner[6], Alexander A. High[2,7], David A. Muller[4,8], Robert Hovden [3] and Jiwoong Park [1,2,5] ✉

Van der Waals (vdW) solids can be engineered with atomically precise vertical composition through the assembly of layered two-dimensional materials[1,2]. However, the artisanal assembly of structures from micromechanically exfoliated flakes[3,4] is not compatible with scalable and rapid manufacturing. Further engineering of vdW solids requires precisely designed and controlled composition over all three spatial dimensions and interlayer rotation. Here, we report a robotic four-dimensional pixel assembly method for manufacturing vdW solids with unprecedented speed, deliberate design, large area and angle control. We used the robotic assembly of prepatterned 'pixels' made from atomically thin two-dimensional components. Wafer-scale two-dimensional material films were grown, patterned through a clean, contact-free process and assembled using engineered adhesive stamps actuated by a high-vacuum robot. We fabricated vdW solids with up to 80 individual layers, consisting of $100 \times 100\,\mu m^2$ areas with predesigned patterned shapes, laterally/vertically programmed composition and controlled interlayer angle. This enabled efficient optical spectroscopic assays of the vdW solids, revealing new excitonic and absorbance layer dependencies in MoS_2. Furthermore, we fabricated twisted N-layer assemblies, where we observed atomic reconstruction of twisted four-layer WS_2 at high interlayer twist angles of $\geq 4°$. Our method enables the rapid manufacturing of atomically resolved quantum materials, which could help realize the full potential of vdW heterostructures as a platform for novel physics[2,5,6] and advanced electronic technologies[7,8].

Precise three-dimensional (3D) spatial control (x, y, z) of the structure and chemical composition of inorganic crystalline materials such as silicon is the foundation for integrated circuitry. van der Waals (vdW) solids formed by stacking two-dimensional materials (2DMs) are not limited by lattice commensurability or interlayer bonding, and, therefore, exhibit two advantages over conventional, sequentially deposited crystals[1,2]. First, lattice and chemical flexibility between adjacent layers means that one can produce arbitrary vertical sequences of crystal compositions with layer-tunable electrical[4,5,9], magnetic[9,10] and optoelectronic[11–14] properties. Second, this interlayer flexibility introduces an additional dimension of θ, the interlayer lattice rotation or twist, as a new degree of freedom for controlling the properties of vdW solids. This has been seen in recent demonstrations of momentum-space crystal engineering and superconductivity of twisted bilayer[4,5,9,15] and trilayer[16] 2DMs. Such advantages are complementary to conventional methods of 3D control by patterning/deposition and provide a powerful approach for producing solids whose properties can be systematically and precisely designed. Realizing these characteristics of a designer solid requires accurate placement of many 2DM pixels (that is, discrete components, not necessarily square-shaped) at target positions (x, y, z) with a specified interlayer angular orientation (θ; Fig. 1a). A method that could achieve this would enable the production of 3D, monolithically integrated solids with parameters such as layer number (N), chemical composition and crystalline structure that are programmatically dictated and controlled.

However, current 2DM processing techniques provide only partial control (principally z and θ) with limited throughput. Conventional 2DM vdW heterostructure assembly relies on irregularly shaped mono- and multilayers isolated through micromechanical exfoliation[1]. Although exfoliated materials maintain remarkable quality, their inherent stochastic distribution and small area do not permit the facile production of integrated solids. Emerging wafer-scale growth by chemical vapour deposition (CVD)[17], metal–organic CVD (MOCVD)[18], controlled recrystallization[19] and solution-based techniques[20] has brought us closer to vdW solid manufacturing, with electronic properties in the best cases rivalling those of exfoliated materials[17].
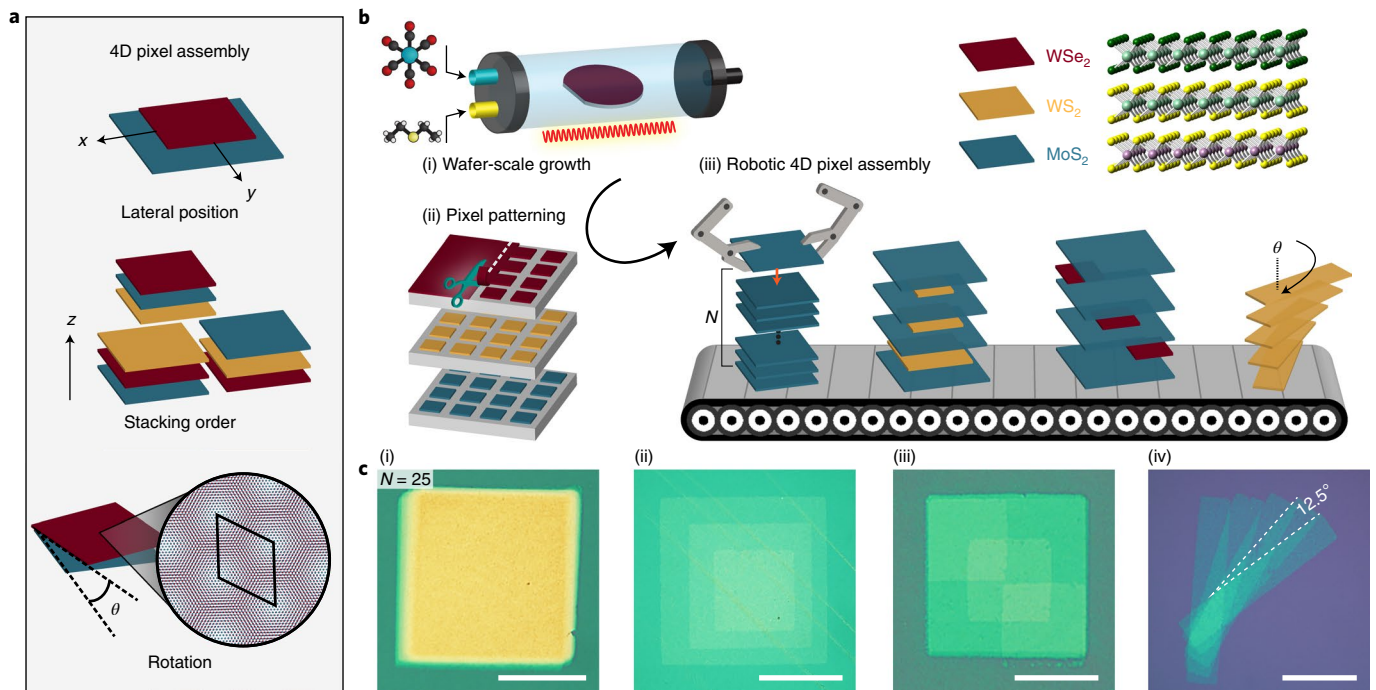
Here we present a versatile high-throughput approach for producing designer vdW solids with full four-dimensional control of x, y, z and θ, as illustrated in Fig. 1b. To achieve this, we combined the wafer-scale synthesis of various 2DMs with two further technical advances: a contact-free patterning technique to mass produce pixel building blocks from the wafer-scale synthesized 2DMs and a high-throughput, operator-free robotic four-dimensional (4D) pixel assembly manufacturing system to assemble these pixels under high vacuum. During the assembly step, multiple pixels, each with a predesigned shape, were chosen and stacked with a precise spatial resolution (x and y), atomic-scale layer control (z and N) and angle resolution (θ).

The versatility of our method enables the design and production of a variety of integrated vdW solids. Figure 1b(iii) illustrates four conceptual structures realized by our robotic 4D pixel assembly (see the micrographs in Fig. 1c): a large N stack (25 layers of MoS_2),

Fig. 1 | Robotic four-dimensional pixel assembly. a, Schematic of the four-dimensional pixel assembly concept. **b**, Production of pixels by wafer-scale growth (i), pixel patterning (ii) and automated pixel assembly of four conceptual structures by a robotic instrument (iii). **c**, Corresponding micrographs of vacuum-assembled robot-manufactured vdW solids demonstrating layer number (i), composition (ii), lateral position (iii) and interlayer twist angle control (iv). All scale bars, 50 μm.

an alternating superlattice with shrinking pixel size of the alternate layer (MoS_2/WS_2), an offset heterostructure with three smaller pixels diagonally aligned (MoS_2/WSe_2) and a 'spiral staircase' with a constant interlayer twist (WS_2, $\theta = 12.5°$). Our deterministic and consistent technique allows us to manufacture these structures at rates in the order of 30 layers per hour (Supplementary Table 1), substantially faster than for state-of-the-art exfoliated materials[21]. At the same time, our technique preserves the quality of the starting material, as demonstrated by the narrow linewidths observed in the cryogenic photoluminescence of exfoliated samples (Supplementary Fig. 1). In the following text, we explain our method in more detail and present two applications realized using the designer vdW solids that we generated using polycrystalline monolayers (Figs. 1–3) and a single crystalline monolayer (Fig. 4).

The core fixture of our robotic 4D pixel assembly process is our vacuum assembly robot (VAR; Fig. 2a and Supplementary Fig. 2). It consists of a heated x–y translation stage that holds multiple ~1 cm^2 chips of source material or receiving substrates, and a separate z–θ actuated stacking platform, which moves a microstructured polymer stamp (Fig. 2b) to pick up the 2DM to form the stack. The VAR is housed within a desktop-size high-vacuum chamber ($P_{base} \approx 10^{-6}$ torr) to reduce surface contamination, prevent material oxidation and promote high-quality interfaces during assembly. An external optical microscope and digital camera directed through the top viewport enable lateral alignment and process monitoring, including detection of the stamp–substrate contact to prevent excessive force (Supplementary Fig. 3). In the manufacturing process the VAR performs two sequential steps (Fig. 2c):

(1) During assembly, the VAR cycles by (a) navigating the stamp to the selected pixel for pick-up, (b) placing the stamp in contact with the pixel and (c) lifting to pick up the target layer. This process repeats to add additional layers to the stamp.

(2) The terminal deposition step involves (a) navigating the stamp to a desired location on the target substrate, (b) contacting the target point with an applied release stimulus, typically heat, and (c) releasing the assembled vdW solid by slowly lifting the z stage.

A multicomposition polymer stamp (Fig. 2b) plays a key role during these two steps. It is specifically designed to exhibit optimal mechanical properties and thermally switched adhesion determined by the glass transition temperature[22], thermolytic release layer decomposition[23] and viscoelastic relaxation[24]. Details of the VAR assembly process and stamp fabrication are given in the Methods and Supplementary Information. The VAR assembly process works for transition metal dichalcogenides (TMDs), Au thin films (Supplementary Fig. 5), exfoliated flakes of graphite, hexagonal boron nitride (hBN; Supplementary Fig. 6) and WSe_2 (Supplementary Fig. 1), and is expected to be applicable to a variety of materials compatible with vdW stacking[7,20,25,26]. Furthermore, the VAR can be used to produce high-quality vdW heterostructures from exfoliated flakes, such as hBN-encapsulated WSe_2, which shows narrow linewidth cryogenic photoluminescence spectra similar to those from manually stacked samples (Supplementary Fig. 1).

This manufacturing process is computer-controlled and the full process, from pick-up of the first layer (1 L) to the transfer of the completed vdW solid, can be fully automated to take advantage of wafer-scale synthetic monolayers. Examples of an automated recipe-driven process are shown in Fig. 3c and Supplementary Video 1. One immediate advantage of automation is its high throughput. This is highlighted by the operator-free fabrication of the 80-layer MoS_2 (Supplementary Fig. 7). For this structure, assembly by traditional manual or semi-automated methods would be tedious and challenging.

The other key technical advance is the fabrication of patterned 2DM building blocks (Fig. 1b(ii)) by a clean, non-perturbative
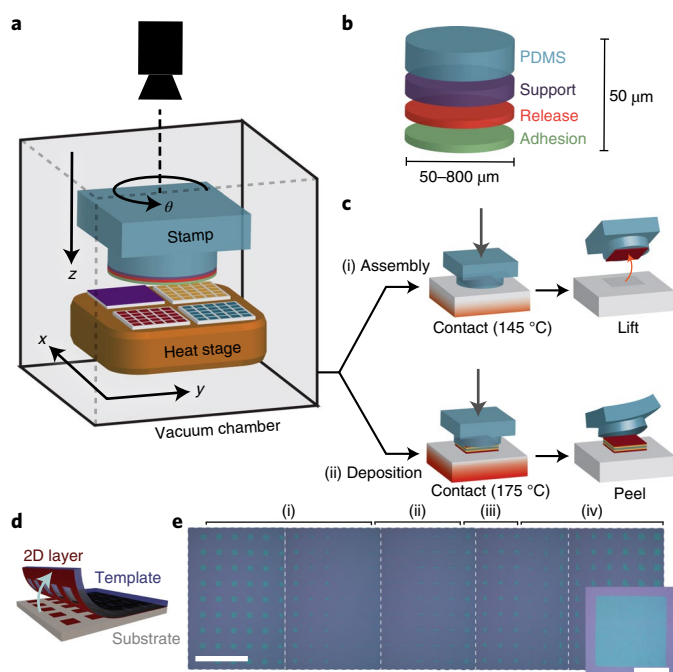
Fig. 2 | Automated vacuum assembly of vdW heterostructures. a, Diagram of the VAR for vdW heterostructure fabrication. **b**, Schematic of the adhesive stamp structure. The multilayer structure mediates programmed adhesion and deposition by thermal and/or UV light activation of the release layer to generate rapid decomposition. Details of the polymer stamp construction are included in the Methods. **c**, Process flow chart demonstrating the steps for the assembly (i) and deposition (ii) of heterostructures on a receiving substrate. **d**, Schematic of the TSL process. **e**, Stitched optical micrographs from $13 \times 13\,mm^2$ chip of square (i), rectangle (ii), triangle (iii) and tiled (iv) WS_2 pixels produced by TSL. Scale bar, 1 mm. Inset: optical micrograph of an individual square pixel. Scale bar, 50 μm.

lithographic technique. Conventional photo- or electron-beam lithography processes involve contact with polymers, chemical developers and solvents, which contaminate vdW interfaces[27]. Instead, we used template strip lithography (TSL), an adhesion-based[22,28], dry patterning technique for 2DMs (see schematic in Fig. 2d) that prevents the deposition of surface residues by not touching the pixel region with the patterning medium. It uses a microstructured template with patterned adhesive regions produced by a standard cleanroom lithography; these adhesive regions stick to the 2DM areas, which are then cleaved and stripped away when the template is lifted from the surface leaving non-contacted 2DM regions behind to generate patterned arrays of 2D pixels. Optical images of an example array made from monolayer WS_2 are shown in Fig. 2e, and an MoS_2 array in Supplementary Fig. 8, which show a high yield of 99%. Atomic force microscopy (AFM) and optical microscopy confirmed clean surfaces with no polymer residues after patterning (Supplementary Figs. 8 and 9).

The precise grid spacing within each patterned chip facilitates the calculation of the spatial coordinates of every pixel (Fig. 2e and Supplementary Fig. 8). It is therefore no longer necessary to individually search, locate, catalogue and characterize the thickness of stochastically exfoliated materials; we can predesign the structure of the incorporated layers. With this deterministic material source as input, the VAR software can interpret scripted recipes of coordinates and stacking conditions to sequentially pick up pixels and manufacture a programmed vdW solid. This differentiates our robotic 4D pixel assembly process from conventional exfoliated 2DM stacking. Spatially resolved measurements, including

confocal laser microscopy (Supplementary Fig. 10) and Raman spectroscopic mapping (Supplementary Fig. 11), can be used to confirm the uniformity of our assembled samples. We designed and conducted two such experiments realized using custom-produced vdW solids: a comprehensive optical assay of N-layer stacked MoS_2 (Fig. 3) and structural characterization of angle-controlled four-layer WS_2 (Fig. 4).

The first experiment is illustrated in Fig. 3 for a MoS_2 solid ($100 \times 100\,\mu m^2$) that consists of 16 square regions, each with a different N ranging from 1 to 16 (see the optical image in Fig. 3a). This 16-tile configuration is specifically designed for the one-shot characterization of the N-dependent evolution of the properties of polycrystalline 2DMs where every interlayer interface has random interlayer rotation. Such information cannot be easily obtained from other samples, such as randomly sized exfoliated flakes[29,30] or multiple samples with statistical thickness fluctuations produced by thin-film growth[31,32]. The structure consists of a stack of 16 Tetris-like pixels (Fig. 3b); each pixel is specifically patterned, then assembled layer-by-layer (see Fig. 3c for the images collected during assembly, and Supplementary Video 1) according to the overall design of the solid. The 16-tile solid in this case has been deposited onto a uniform MoS_2 substrate layer to yield a structure with 1–17 layers (the monolayer properties can be probed outside the tiled region). The high quality of the interlayer interfaces was confirmed by cross-sectional scanning transmission electron microscopy (STEM) images (Fig. 3d) taken from different regions (thus different N values) of another similarly produced sample.

Using hyperspectral microscopy, we measured the transmission (T) and reflection (R) images of this solid at different wavelengths (λ) after the sample had been transferred to a sapphire substrate. Example images ($\lambda = 680\,nm$) are presented in Fig. 3e and show uniform contrast in each tile region. By comparing these images with substrate and mirror reference images, we measured the reflection ($R(\lambda, N)$) and absorption ($A(\lambda, N) = 1 - T - R$) spectra of the 16-tile optical assay, each averaged over one tile region. The resulting absorption spectra for $N = 1$–17 are shown in Fig. 3f and display a layer-dependent evolution of the peak positions and magnitude. Despite the random interlayer orientations present in our sample, these spectra show two clearly resolved absorption peaks near the A and B exciton energies. The fitted peak positions (Fig. 3g) for smaller N are close to the values previously observed in mono- and bilayer MoS_2 (ref. [33]), and they then decrease and converge near the values of bulk 2H MoS_2 (ref. [30]). This suggests that the intralayer direct-gap K–K (or K′–K′) transition, which is insensitive to interlayer rotations, remains dominant in our stacked MoS_2 solid. This also suggests that the magnitude of $R(\lambda, N)$ and $A(\lambda, N)$ for stacked MoS_2 can be understood for different N using a simple model without explicitly considering the interlayer rotation angles. We find that this is indeed the case: the absorption spectra in Fig. 3f can be closely matched for all N using a simple transfer matrix method (TMM)[34] calculation based on monolayer optical constants as the building blocks (Supplementary Fig. 12). Such insensitivity of R and A to the interlayer rotations has practical implications, as it allows for modelling stacked MoS_2 films as a single material for photonic applications. Another finding is that the reflectance (R) converges to the 3D-bulk-crystal limit quickly for thin MoS_2 films: even at $N = 17$ (thickness ≈ 10 nm), the stacked film reflects approximately 40% of incoming light on average (Supplementary Fig. 12), close to the reflectivity of bulk MoS_2.

The photoluminescence (PL) from the 16-tile optical assay (Fig. 3g,h) also shows N-dependent evolution. There is an 87% decrease in the integrated intensity of the main A exciton peak from 1 L to 2 L (Supplementary Fig. 13), which is comparable to other stacked bilayer samples[35,36] and explained by a direct-to-indirect gap transition. However, when compared with natural 2H MoS_2 at thicknesses greater than 2 L, our assay shows less PL quenching with
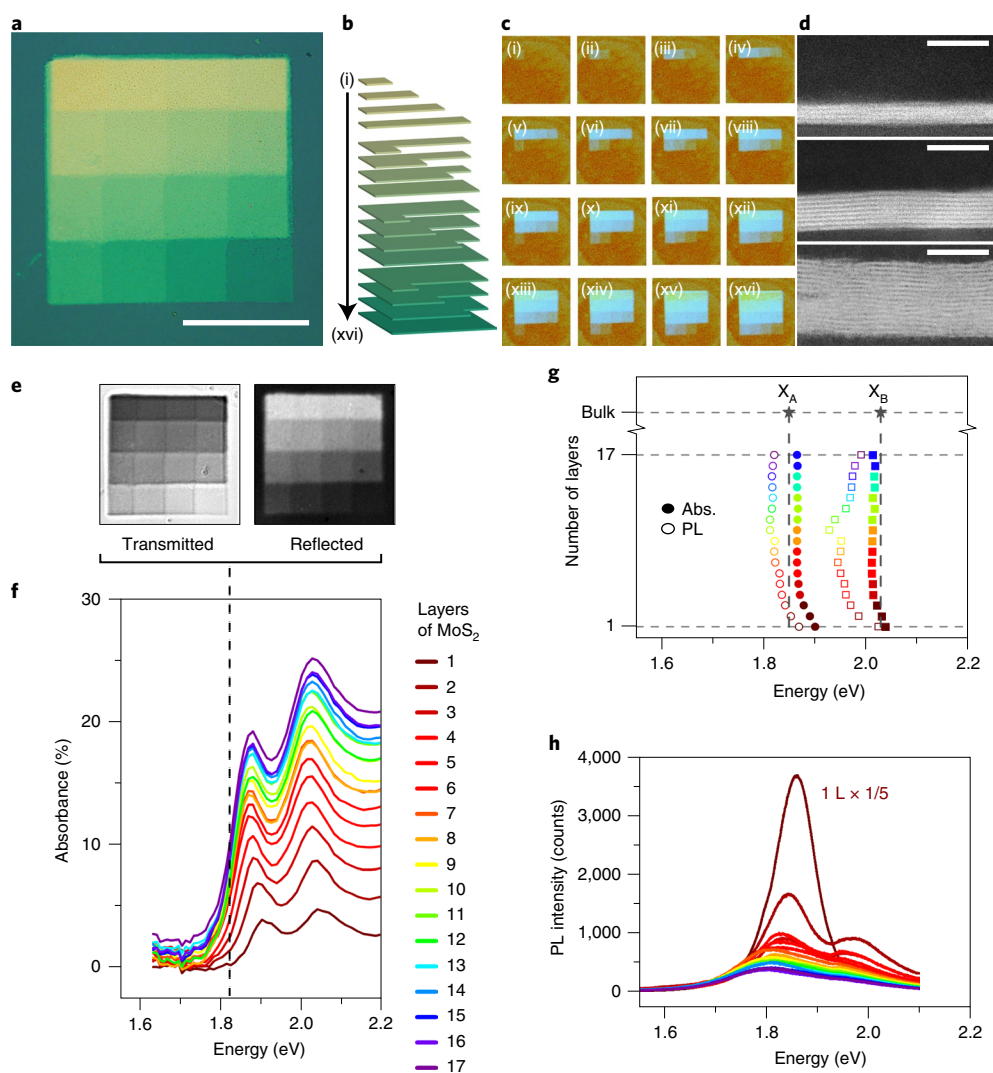
Fig. 3 | Comprehensive optical assay of *N*-layer stacked MoS₂. a, White-light optical micrograph of the 1–16 L MoS₂ grid structure. Scale bar, 50 μm. **b**, Schematic of 16 layers (i)–(xvi) of the structured pixel assembly to realize the 16-tile grid structure. **c**, In situ micrographs of the designed 16-tile heterostructure fabrication. Each image represents a layer (i)–(xvi). The images were taken when the stamp was in contact with the substrate. **d**, Cross-sectional STEM images of 4 L (top), 8 L (middle) and 16 L (bottom) MoS₂ extracted from the design shown in **b**, demonstrating atomically resolved thickness control. All scale bars, 10 nm. **e**, Hyperspectral microscope transmission and reflection images obtained from the sample in **a**, near the onset of the A exciton absorption wavelength (680 nm), demonstrating uniformly increasing contrast for individual layers. **f**, Absorbance spectra acquired from **a** by hyperspectral microscopy. **g**, Plotted curve fits of excitonic peak positions from the optical spectroscopy data, with bulk 2H MoS₂ absorbance peaks extracted from the literature[30] shown as filled stars and labelled X_A and X_B for the A and B exciton energies, respectively. The vertical dashed lines mark the bulk exciton peak positions to guide comparison with experimental data, and the horizontal dashed lines indicate layer number values of 1 L, 17 L and bulk thickness on the y axis. **h**, Photoluminescence spectra of 1–17 L MoS₂ acquired from **a**.

increasing *N* and a broadening of the direct A exciton transition peak[37]. Both observations may result from the modified interlayer hybridization present in the rotationally misaligned layers and multiple domains contributing to the observed signal. Finally, we note that we observe one *N*-dependent effect in all our measured spectra (*R*, *A* and PL): as *N* increases from 1 to ~5, gradual redshifts of both the A and B exciton peaks are observed, which occurs due to enhanced screening[38].

Our second experiment is demonstrated in Fig. 4 for a multilayer WS₂ solid with precise interlayer rotations. It showcases the angle control of our robotic stacking system. This is an important new capability for designing 2DM-based solids with strongly correlated electronic and excitonic states[2,5]. Figure 4a shows a selected area electron diffraction (SAED) pattern for a four-layer WS₂ sample, obtained by our nanomanufacturing technique using a large

triangular single crystal of WS₂ (~100 μm side length) grown by MOCVD (inset) as the source. The single crystallinity of this source material is discussed further in Supplementary Fig. 14. Different regions of this triangular single crystal of WS₂ were picked up using our stamp, piece by piece, with interlayer rotation applied between each layer. This technique allows us to generate multilayer twisted heterostructures, with every interlayer rotation angle controlled. This method can be applied generally to form more complex stacks using larger single-crystalline[39] or lattice-oriented[40] 2DM sources.

The diffraction pattern in Fig. 4a clearly shows four sets of primary Bragg peaks, each rotated slightly from the neighbouring ones. All three interlayer twist angles (θ_{12}, θ_{23} and θ_{34}) are close to 4.2° (mean of 4.2 ± 0.2°), with θ_{12} being larger than the other two. The precision of the rotation angle realized in our stack is currently limited by the open-loop mechanical resolution of our angle
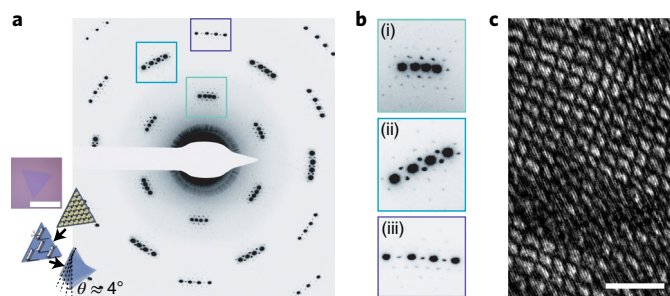
Fig. 4 | Reconstruction in twisted four-layer WS₂. a, SAED pattern acquired via TEM from a 4 L structure of WS₂ with a twist angle of $4.2 \pm 0.2°$ between adjacent layers. Inset: schematic showing the manufacture of a twisted heterostructure from a single crystal of monolayer WS₂, and an optical micrograph of a single-crystal WS₂ triangle. Scale bar, 100 μm. **b**, Magnified views of superlattice peaks for first-order (i), second-order (ii) and third-order (iii) sets of diffraction spots, showing prominent satellite peaks associated with interlayer atomic reconstruction. **c**, A DF-TEM image with the objective aperture placed over a set of second-order Bragg peaks, showing evidence of atomic reconstruction, with the larger 'fishnet' domains attributed to the ~4° twist angle between the innermost layers and the high-frequency stripes corresponding to the ~12° twist angle between the outermost layers. Scale bar, 40 nm.

actuator ($\pm 0.2°$; Supplementary Fig. 15), although there could be additional contributions from unintentional movement of each 2DM piece induced during and after the pick-up, and small orientation variation within the single-crystal source materials.

Surprisingly, we observe strong satellite peaks beyond the primary Bragg peaks, as shown by the magnified images in Fig. 4b. Figure 4c shows a dark-field transmission electron microscopy (DF-TEM) image obtained by selecting the second-order Bragg peaks and surrounding satellites (Fig. 4b(ii)). Larger 'fishnet' domains separated by dark boundaries are clearly visible in this image, with their spatial period (of the order of 10 nm) corresponding to the moiré wavelength for $\theta \approx 4°$. Multislice simulation of a rigid 4.2° twisted four-layer WS₂ structure (Supplementary Fig. 16) indicates that satellite peaks arising from multiple scattering would have a nearly undetectable signal, therefore the apparent satellite peaks in Fig. 4a,b must be evidence of atomic reconstruction[41,42]. We measured the intensity ratio between the main Bragg peaks and the primary satellite peaks to be 1–2% (Supplementary Fig. 17), nearly twice what would be expected from rigid lattice multiple scattering. We also observe in Fig. 4c a superimposed striped pattern. This corresponds to the moiré wavelength of the outer two layers, $3\theta \approx 12°$. Together, the fishnet and striping domains indicate that it is likely that the inner two layers are restructuring. However, it is as yet unclear whether the reconstruction occurs solely from the interactions between the interior two layers, or whether there are cooperative multilayer interactions. We will seek to elucidate the nature of such N-layer twisted interactions in future work.

Our observation of lattice restructuring at $\theta \approx 4.2°$ is unexpected. The lattice reconstruction is driven by a reduction in interfacial energy, which is proportional to the size of the reconstructed domain. As the domain size is inversely proportional to twist angle, reconstruction due to interlayer interactions has previously been observed at smaller twist angles (for example, up to ~3° for graphene[41], ~2° for TMDs[42]). However, modified interlayer mechanical coupling[43] and strongly correlated states[15] have been observed at twist angles up to ~5° in bilayer TMDs, underscoring the importance of understanding the atomic reconstruction in these materials. Moreover, atomic-scale engineered chirality[44] applied to 2D semiconductors may potentially enable efficient photonic and quantum

information processing by enhancing the coupling between light helicity and valley polarization[45], or by enhancing non-linear optical phenomena[46].

Robotic 4D pixel assembly presents a new method for manufacturing precise vdW solids, highlighted by our two demonstrations of a one-shot optical assay and twisted multilayer stacking. Some limitations of the VAR, namely lateral and angular resolution, could be improved by using higher-specification closed-loop actuators. The lateral size of the assembled area can be increased by developing a larger stamp that can make contact with optimal and uniform force (Supplementary Fig. 19). Strain formation, especially at high layer counts, could be reduced by minimizing unconstrained thermomechanical stresses on the 2DM–polymer interface (Supplementary Discussion). Our large sample size and predominantly monolayer source material are challenging compared with the common practice of using a thicker flake of hBN as the top layer, which acts as a mechanical buffer layer and decouples the heterostructure from slight mechanical deformation imparted by the polymeric stamp. Contrasting with existing fabrication methods based on exfoliated materials (where each device is unique), our manufacturing process could enable the efficient assembly of identical structures on the same chip. When combined with the growth of large single crystals of 2DMs, our assembly technique could enable high-throughput investigation of engineered electronic states in more complex, multilayer twisted heterostructures[16]. This also establishes an avenue for harnessing twisted structures in technological applications. Moreover, beyond wafer-scale synthesized TMDs, the processes of large-area material synthesis, precise patterning and automated assembly should generalize to other categories of delaminable materials, such as thin-film electrodes[25], 2D complex oxides[26,47] or molecular monolayers[20].

Online content

Any methods, additional references, Nature Research reporting summaries, source data, extended data, supplementary information, acknowledgements, peer review information; details of author contributions and competing interests; and statements of data and code availability are available at https://doi.org/10.1038/s41565-021-01061-5.

References

1. Geim, A. K. & Grigorieva, I. V. Van der Waals heterostructures. *Nature* **499**, 419–425 (2013).
2. Song, J. C. W. & Gabor, N. M. Electron quantum metamaterials in van der Waals heterostructures. *Nat. Nanotechnol.* **13**, 986–993 (2018).
3. Kim, K. et al. van der Waals heterostructures with high accuracy rotational alignment. *Nano Lett.* **16**, 1989–1995 (2016).
4. Cao, Y. et al. Unconventional superconductivity in magic-angle graphene superlattices. *Nature* **556**, 43–50 (2018).
5. Balents, L., Dean, C. R., Efetov, D. K. & Young, A. F. Superconductivity and strong correlations in moiré flat bands. *Nat. Phys.* **16**, 725–733 (2020).
6. Tang, Y. et al. Simulation of Hubbard model physics in WSe₂/WS₂ moiré superlattices. *Nature* **579**, 353–358 (2020).
7. Liu, Y., Huang, Y. & Duan, X. Van der Waals integration before and beyond two-dimensional materials. *Nature* **567**, 323–333 (2019).
8. Akinwande, D. et al. Graphene and two-dimensional materials for silicon technology. *Nature* **573**, 507–518 (2019).
9. Lu, X. et al. Superconductors, orbital magnets and correlated states in magic-angle bilayer graphene. *Nature* **574**, 653–657 (2019).
10. Sharpe, A. L. et al. Emergent ferromagnetism near three-quarters filling in twisted bilayer graphene. *Science* **365**, 605–608 (2019).
11. Rivera, P. et al. Interlayer valley excitons in heterobilayers of transition metal dichalcogenides. *Nat. Nanotechnol.* **13**, 1004–1015 (2018).
12. Tran, K. et al. Evidence for moiré excitons in van der Waals heterostructures. *Nature* **567**, 71–75 (2019).
13. Shimazaki, Y. et al. Strongly correlated electrons and hybrid excitons in a moiré heterostructure. *Nature* **580**, 472–477 (2020).

14. Alexeev, E. M. et al. Resonantly hybridized excitons in moiré superlattices in van der Waals heterostructures. *Nature* **567**, 81–86 (2019).
15. Wang, L. et al. Correlated electronic phases in twisted bilayer transition metal dichalcogenides. *Nat. Mater.* **19**, 861–866 (2020).
16. Park, J. M., Cao, Y., Watanabe, K., Taniguchi, T. & Jarillo-Herrero, P. Tunable strongly coupled superconductivity in magic-angle twisted trilayer graphene. *Nature* **590**, 249–255 (2021).
17. Banszerus, L. et al. Ultrahigh-mobility graphene devices from chemical vapor deposition on reusable copper. *Sci. Adv.* **1**, e1500222 (2015).
18. Kang, K. et al. High-mobility three-atom-thick semiconducting films with wafer-scale homogeneity. *Nature* **520**, 656–660 (2015).
19. Xu, X. et al. Seeded 2D epitaxy of large-area single-crystal films of the van der Waals semiconductor 2H MoTe$_2$. *Science* **372**, 195–200 (2021).
20. Zhong, Y. et al. Wafer-scale synthesis of monolayer two-dimensional porphyrin polymers for hybrid superlattices. *Science* **366**, 1379–1384 (2019).
21. Masubuchi, S. et al. Autonomous robotic searching and assembly of two-dimensional crystals to build van der Waals superlattices. *Nat. Commun.* **9**, 1413 (2018).
22. Pizzocchero, F. et al. The hot pick-up technique for batch assembly of van der Waals heterostructures. *Nat. Commun.* **7**, 11894 (2016).
23. Fritz, N., Dao, H., Allen, S. A. B. & Kohl, P. A. Polycarbonates as temporary adhesives. *Int. J. Adhes. Adhes.* **38**, 45–49 (2012).
24. Castellanos-Gomez, A. et al. Deterministic transfer of two-dimensional materials by all-dry viscoelastic stamping. *2D Mater.* **1**, 011002 (2014).
25. Liu, Y. et al. Approaching the Schottky–Mott limit in van der Waals metal–semiconductor junctions. *Nature* **557**, 696–700 (2018).
26. Kum, H. S. et al. Heterogeneous integration of single-crystalline complex-oxide membranes. *Nature* **578**, 75–81 (2020).
27. Lin, Y.-C. et al. Graphene annealing: how clean can it be? *Nano Lett.* **12**, 414–419 (2012).
28. Nagpal, P., Lindquist, N. C., Oh, S.-H. & Norris, D. J. Ultrasmooth patterned metals for plasmonics and metamaterials. *Science* **325**, 594–597 (2009).
29. Hsu, C. et al. Thickness-dependent refractive index of 1L, 2L, and 3L MoS$_2$, MoSe$_2$, WS$_2$, and WSe$_2$. *Adv. Opt. Mater.* **7**, 1900239 (2019).
30. Morozov, Y. V. & Kuno, M. Optical constants and dynamic conductivities of single layer MoS$_2$, MoSe$_2$, and WSe$_2$. *Appl. Phys. Lett.* **107**, 083103 (2015).
31. Song, B. et al. Complex optical conductivity of two-dimensional MoS$_2$: a striking layer dependency. *J. Phys. Chem. Lett.* **10**, 6246–6252 (2019).
32. Ji, H. G., Solís-Fernández, P., Erkılıç, U. & Ago, H. Stacking orientation-dependent photoluminescence pathways in artificially stacked bilayer WS$_2$ nanosheets grown by chemical vapor deposition: implications for spintronics and valleytronics. *ACS Appl. Nano Mater.* **4**, 3717–3724 (2021).
33. Niu, Y. et al. Thickness-dependent differential reflectance spectra of monolayer and few-layer MoS$_2$, MoSe$_2$, WS$_2$ and WSe2. *Nanomaterials* **8**, 725 (2018).
34. Havener, R. W. et al. Hyperspectral imaging of structure and composition in atomically thin heterostructures. *Nano Lett.* **13**, 3942–3946 (2013).
35. Huang, S. et al. Probing the interlayer coupling of twisted bilayer MoS$_2$ using photoluminescence spectroscopy. *Nano Lett.* **14**, 5500–5508 (2014).
36. Liu, K. et al. Evolution of interlayer coupling in twisted molybdenum disulfide bilayers. *Nat. Commun.* **5**, 4966 (2014).
37. Mak, K. F., Lee, C., Hone, J., Shan, J. & Heinz, T. F. Atomically thin MoS$_2$: a new direct-gap semiconductor. *Phys. Rev. Lett.* **105**, 136805 (2010).
38. Raja, A. et al. Dielectric disorder in two-dimensional materials. *Nat. Nanotechnol.* **14**, 832–837 (2019).
39. Chubarov, M. et al. Wafer-scale epitaxial growth of unidirectional WS$_2$ monolayers on sapphire. *ACS Nano* **15**, 2532–2541 (2021).
40. Liao, M. et al. Precise control of the interlayer twist angle in large scale MoS$_2$ homostructures. *Nat. Commun.* **11**, 2153 (2020).
41. Yoo, H. et al. Atomic and electronic reconstruction at the van der Waals interface in twisted bilayer graphene. *Nat. Mater.* **18**, 448–453 (2019).
42. Weston, A. et al. Atomic reconstruction in twisted bilayers of transition metal dichalcogenides. *Nat. Nanotechnol.* **15**, 592–597 (2020).
43. Quan, J. Phonon renormalization in reconstructed MoS$_2$ moiré, superlattices. *Nat. Mater.* **20**, 1100–1105 (2021).
44. Kim, C.-J. et al. Chiral atomically thin films. *Nat. Nanotechnol.* **11**, 520–524 (2016).
45. Scuri, G. et al. Electrically tunable valley dynamics in twisted WSe$_2$/WSe$_2$ bilayers. *Phys. Rev. Lett.* **124**, 217403 (2020).
46. Yao, K. et al. Enhanced tunable second harmonic generation from twistable interfaces and vertical superlattices in boron nitride homostructures. *Sci. Adv.* **7**, eabe8691 (2021).
47. Lu, D. et al. Synthesis of freestanding single-crystal perovskite films and heterostructures by etching of sacrificial water-soluble layers. *Nat. Mater.* **15**, 1255–1260 (2016).

Methods

Wafer-scale TMD synthesis. Monolayer TMDs (MoS$_2$, WS$_2$ and WSe$_2$) were synthesized using MOCVD, as established in prior work[18]. Unless noted otherwise, samples were polycrystalline thin films, composed of complete monolayers or slightly overgrown monolayers (having some small bilayer regions nucleated at grain boundaries). Silicon wafers with a 300-nm thermal oxide layer were used as growth substrates. Materials were verified to be continuous by AFM prior to use.

Template strip lithography patterning. Polydimethylsiloxane (PDMS) patterned blocks were used for the majority of the TSL patterning in this work, with voids for the non-contact regions. The moulds for casting PDMS TSL templates were fabricated through standard microfluidics techniques. A SU8-3050 photoresist was spin-coated on 75 mm silicon wafers, lithographically patterned, hard-baked and silanized with trimethylchlorosilane. PDMS (Sylgard-184) was then poured into the SU8 moulds and cured on a level surface for 2 days at room temperature.

For patterning MOCVD TMDs, a MOCVD growth wafer was first cleaved into ~1 cm^2 chips. A PDMS TSL block was cut to roughly the same size as the chip cleaved for patterning, then gently placed onto the material such that the patterned relief faces the material. This structure was exposed to steam for 4–8 s, then immediately after, the TSL block was peeled off the chip. After peeling, the pattern had transferred to the material. This method is extremely fast and the PDMS moulds are reusable. It was used for the samples in Figs. 1c(i),(iii) and 3.

Another method for TSL patterning uses patterned metal thin films (non-adhesive to 2DMs) embedded in a poly(methyl methacrylate) (PMMA) thin film (adhesive to 2DMs). This method was used for patterning the samples shown in Figs. 1c(ii),(iv) and 2e.

Our patterning process was performed as follows. (1) We used cleanroom photolithography to produce a flexible, structured template with an atomically flat bottom surface and spatially patterned regions of strong adhesion. (2) We applied this adhesive template to the 2DM to achieve uniform contact between the adhesive regions and the sample, then peeled off the template. This resulted in the cleavage and removal of the 2DM from the adhesive regions, leaving behind pixels of patterned material. The patterns in these templates are defined by the non-adhesive regions, voids or inert materials, with negligible adhesion to 2DMs. In principle, the adhesive force can be widely tuned to accommodate various 2DM/substrate combinations through the use of different polymers or the addition of intercalant species (for example, H$_2$O).

Polymer stamp fabrication. The stamp was carefully designed to modulate substrate–layer–stamp adhesion. The lift rate affects the viscoelastic response of the polymer stamp, which manifests as high adhesion when the stamp is lifted from the substrate quickly or low adhesion when peeled off slowly. The temperature dictates adhesion through polymer reflow when the glass transition temperature is exceeded, or release when the decomposition temperature of the release layer is reached.

The stamp begins as a cylindrical PDMS base (diameter 50–800 μm), cast using a similar technique to that for the TSL patterns. A different PDMS formulation, MasterSil 971-LO, was used for its low outgassing properties. The subsequent polymer layers were all applied to the cast and cured PDMS by spin-coating at 2,000 r.p.m. for 1 min. Optical micrographs of the bottom surface of a poor- and high-quality stamp are shown in Supplementary Fig. 4.

Structural integrity is provided by a layer of MicroChem Lift-Off Resist (LOR10B). Its high glass transition temperature (190 °C) ensures physical rigidity during the assembly process. This layer improves the surface quality of the assembled vdW heterostructures by reducing small-scale surface wrinkles.

The next polymer layer is the release layer, consisting of poly(cyclohexene propylene carbonate) (PCPC) with added photoacid generator to assist in controlled decomposition and adhesion release. The PCPC is dissolved at 6 wt% in anisole, with the photoacid generator mixed in at 5% of the PCPC mass. The photoacid compound is activated when exposed to either ultraviolet light or elevated temperature (175 °C), thereby initiating degradation of the release layer and physically separating the two surrounding polymer layers.

The final layer is poly(benzyl methacrylate) (PBzMA), dissolved at 6 wt% in anisole. PBzMA has a low glass transition temperature (50 °C). The VAR operates above the PBzMA glass transition during heterostructure assembly, allowing this layer to relax into conformal contact when pressed against a targeted vdW material.

VAR system construction. The vacuum chamber was built from modular components from Ideal Vacuum and the motorized navigation stages were assembled using Newport vacuum-compatible actuators and stages. A variable-magnification microscope (×2 to ×30) was directed through the top viewport of the vacuum chamber. The heating stage consisted of a vacuum-compatible resistive heater–thermoelectric cooler combination to provide fast and reproducible control over the sample temperature. The stage actuation, image acquisition and system temperature were controlled using LabVIEW (https://www.ni.com/).

General VAR manufacturing process. Chips of source material were first patterned by TSL and imaged under an Olympus BX51, OLS 5000 LEXT (405 nm

laser illumination) or DSX1000 microscope to confirm high-quality patterning before insertion into the VAR.

Prior to assembly, the VAR was equipped with a polymer stamp, chips of patterned material and a final transfer substrate. Then, the system was pumped down to high vacuum. The VAR assembly process was realized as follows:

(1) The translation stage shifts to the user-programmed 'pixel' of the patterned material.
(2) The imprint platform lowers the polymer stamp towards the targeted pixel as an image processing algorithm runs over the in situ camera view (see Fig. 2c(i) and Supplementary Fig. 2).
(3) When the transparent stamp contacts the substrate, a change in colour contrast is detected and the stamp approach is halted (Supplementary Fig. 3b).
(4) The stamp is held in contact with the heated substrate (145 °C) for 60 s. During the hold period, the polymer adhesion layer relaxes into nanoscale conformal contact. Optionally, the stage temperature can be lowered to around the transition glass temperature of the adhesion or release layer to reduce the deformation upon separation.
(5) The imprint platform rapidly shifts upwards (100 μm at nominally 2,000 μm s^{-1}) and the material is picked up from the substrate onto the stamp.

This approach–hold–lift loop was executed for all layers programmed into the assembly instruction file. After the heterostructure assembly was complete, the vdW solid was delaminated from the stamp onto a final transfer substrate. Various final substrates were used, including native oxide silicon, 300-nm silicon oxide, sapphire and unpatterned MOCVD TMDs. The VAR was programmed to execute a different operational protocol for final release, as follows:

(1) The stamp is brought into contact with the final substrate at the regular stacking temperature. This minimizes thermal expansion mismatch at the onset of stamp contact.
(2) The translation stage is heated to 175 °C to activate the photoacid generator in the release layer (Fig. 2c(ii)).
(3) After 5 min, the release layer is sufficiently degraded and the VAR slowly raises the stamp from the substrate (200 nm s^{-1}), transferring the completed heterostructure.

These processes are shown in Supplementary Video 1 at a speed increased 100-fold.

Post-processing manufactured structures. Completed structures from VAR manufacturing were cleaned with solvent (acetone for 45 min or chloroform for ≥10 h) to remove any remaining polymers from the heterostructure surface. Optionally, some were thermally annealed at 300 °C for >6 h.

Focused ion beam 16-tile sample cross-section preparation. The 16-tile MoS$_2$ cross-sections were prepared using a Thermo Fisher Helios G4 UX Focused Ion Beam (FIB). The sample chip was positioned such that cross-sections could be cut perpendicular to the boundaries between squares of different MoS$_2$ layer numbers. Protective layers of carbon (~200 nm) and platinum (~1 μm) were deposited onto the squares expected to have 4, 8 and 15 MoS$_2$ layers. Cross-sections were milled from these regions at a 90° angle from the sample using a Ga ion beam at 30 kV. The cross-sections were then further polished to electron beam transparency with the ion beam at 5 kV.

STEM 16-tile sample cross-section imaging. The cross-sections were imaged in a Thermo Scientific Titan Themis STEM at 120 kV at a probe convergence angle of 21.4 mrad. The high-angle annular dark-field STEM images showed bright bands corresponding to the MoS$_2$ layers and confirmed that the vacuum-assembly technique produced clean stacking and correct layer number in each of the three (4 L, 8 L and 15 L MoS$_2$) cross-sectional samples. All images were analysed using the open-source software Cornell Spectrum Imager[48].

Optical photoluminescence, Raman and hyperspectral transmittance/ reflectance microscopy measurements. The vdW solids were initially transferred by VAR onto a MOCVD MoS$_2$ monolayer on a 300-μm Si/SiO$_2$ substrate. PL of the 16-tile sample (Fig. 3) was recorded on a HORIBA LabRAM HR Evolution Confocal Raman Microscope using a 532 nm laser. A ×50 objective lens was used with a laser spot size of ~2 μm. A PL map of the 16-tile structure was constructed using an x–y step size of 12.5 μm so that four spectra were recorded for each tile position, with eight spectra recorded for the monolayer region. The spectra were recorded at room temperature with a laser power of 0.5 mW for two acquisitions of 1.2 s with a grating of 600 lines mm^{-1}. Voigt distributions with zero background were used to fit the A and B peaks.

For Raman mapping (Supplementary Fig. 11), the MoS$_2$/WSe$_2$ heterostructure and monolayer references were illuminated with a 532 nm laser at 0.25 mW. The spectra were acquired using a ×100 objective lens with a grating of 1,800 lines mm^{-1}. The acquisition time per spectrum was 1.5 s, with each complete map taking 30–40 min. A flat noise baseline was subtracted from each individual spectrum, and the integrated areas of the respective peaks were used to colour the Raman map, normalized such that the minimum/maximum value for each channel was assigned to a minimum/maximum colour intensity, respectively.

For hyperspectral microscopy, the 16-tile structure was transferred onto a 330-μm double-sided polished sapphire substrate by first spin-coating the sample on the original Si/SiO₂ substrate with PMMA, then etching in 1 M KOH to remove the vdW solid from the Si, relocating onto water and finally, controllably water-drain-transferring onto the sapphire. The hyperspectral microscope was built with similar specifications to those reported previously[34], but with slightly modified reflection and transmission objectives for higher resolution. The light source was a Xe bulb and was filtered using a monochromator, with 4 nm spectral resolution. A parallel photodiode was used to monitor the time-dependent Xe signal fluctuation. The photodiode data were used to normalize the signal during separate spectral acquisitions. An Andor iXon+ 885 EMCCD device was used as the 2D imaging detector.

Both the reflection and transmission data were collected with the sample facing the incident light, meaning that the sample had to be flipped over between the two imaging modes. A bare sapphire substrate spectrum was also recorded to extract its optical constant. Transmission in air without the sample, reflection by a silver mirror and background signals without illumination were recorded as the maximum transmission, maximum reflection and noise level, respectively. The background dark signal was first subtracted from the images for each wavelength, which were then transformed into transmittance and reflectance by dividing by the maximum transmission and maximum reflection images, respectively.

Absorption was calculated as:

$$A = -T_0(\mathrm{d}T) - R_0(\mathrm{d}R)$$

where T_0 is defined as $T_{substrate}/T_{air}$, R_0 is $R_{substrate}/R_{mirror}$, $\mathrm{d}T$ is the differential transmission of the sample, given as $(T_{sample} - T_{substrate})/T_{substrate}$, and $\mathrm{d}R$ is the differential reflection, given as $(R_{sample} - R_{substrate})/R_{substrate}$. The A and B peaks were fitted in the 552–708 nm (2.25–1.75 eV) range, with a slanted background on two Voigt distributions for the two peaks.

TMM calculation of optical response. The TMM data were calculated using an air–sample–substrate–air system for direct comparison with the experimental data (Supplementary Fig. 12). The sample portion was treated as individual monolayers (for example, the 3 L MoS₂ region in the 16-tile structure = 1 L MoS₂ + 1 L MoS₂ + 1 L MoS₂).

The optical constant of the 330-μm sapphire substrate was extracted by an inverse TMM solver. This showed a minor wavelength dependence due to slight chromatic aberration in the microscope reflectivity at short wavelengths (400–450 nm). The extracted wavelength-dependent sapphire optical constant was then used for the substrate in the T and R TMM calculations.

Two-dimensional materials isolated by different methods will display variations in their complex optical constants n and k because of differing synthesis or processing methodologies. Variation in n and k can be as much as ±25%, comparing the values in published work[49-51]. The optical constant used for MoS₂ for the TMM calculation was taken from published work[52], with an applied constant prefactor to the n and k values to account for sample variation between our synthesized material and the material used in the published work. The optimal result for matching our monolayer MoS₂ T and R to those of the published reference was achieved by multiplying n by 0.85 and k by 0.70. All TMM code was implemented in MATLAB (https://www.mathworks.com/products/matlab.html).

Twisted 4 L WS₂ fabrication. Large, randomly oriented single crystals of WS₂ were synthesized by MOCVD on Si/SiO₂ substrates. Growth substrates were cleaved into ~1 cm² chips and mounted in the VAR without any TSL patterning. The stamp was used to pick out subsections from a large single crystal, with identical numbers of θ actuator steps taken between layers. The VAR was used in operator-assisted mode for twisted N-layer fabrication. After picking up all the layers, the structure was transferred onto a silicon substrate with a 300-nm oxide layer for inspection. Without further post-processing, the final substrate was spin-coated with PMMA, floated on 1 M KOH and transferred onto a 1-μm holey carbon-coated copper TEM grid. The TEM grid was then cleaned in acetone with a critical point dryer to remove all polymer.

TEM of twisted 4 L WS₂. DF-TEM and SAED of the twisted four-layer WS₂ sample were performed on a TFS Talos instrument (operated at 200 keV) equipped with a Gatan OneView camera. DF-TEM images were obtained by placing an objective aperture around the optic axis and tilting the beam to achieve two-beam conditions around diffraction peaks of interest.

Thin-film source sample preparation. Au thin films with a thickness of 20 nm were deposited onto native oxide-coated Si wafers using an AJA-Orion 8E electron beam evaporation system.

Exfoliated sample preparation and cryogenic photoluminescence measurements. Exfoliated flakes of hBN (HQ Graphene) and WSe₂ (2D Semiconductors) were deposited onto Si/SiO₂ substrates. For the cryogenic experiment (Supplementary Fig. 1), the source flakes were inserted into the VAR and an hBN/WSe₂/hBN stack was fabricated. The sample was subsequently cleaned of polymer residue by solvent washing and thermal annealing, and then

inserted into a closed cycle optical cryostat for measurement at 7 K. For the PL measurements, we excited the sample above the band gap with a diffraction-limited 518 nm pump pulse with a power of ~2 μW. For the differential reflectivity measurements, we used a broadband light-emitting diode light source to measure $\mathrm{d}R = R_{WSe2}/R_{hBN} - 1$, where R_{WSe2} (R_{hBN}) is the reflection from the heterostructure collected from within (outside) the monolayer region.

Laser confocal scanning microscopy. An Olympus OLS 5000 LEXT microscope was used to acquire the images for laser confocal scanning microscopy (Supplementary Fig. 10). A ×20 objective lens was used for the low-magnification white-light images and a ×100 objective lens was used for the high-magnification white-light images and the confocal intensity images. The brightness setting was kept constant for the intensity images. Finally, $30 \times 30\,\mu m^2$ regions of interest centred in the middle of each intensity image was used to create the histograms for the plot in Supplementary Fig. 10d.

Data availability
The data that support the findings of this study are available from the corresponding authors upon reasonable request. Source data are provided with this paper.

Code availability
All code used in this work is available from the corresponding authors upon reasonable request.

References
48. Cueva, P., Hovden, R., Mundy, J. A., Xin, H. L. & Muller, D. A. Data processing for atomic resolution electron energy loss spectroscopy. *Microsc. Microanal.* **18**, 667–675 (2012).
49. Zhang, H. et al. Measuring the refractive index of highly crystalline monolayer MoS₂ with high confidence. *Sci. Rep.* **5**, 8440 (2015).
50. Liu, H.-L. et al. Temperature-dependent optical constants of monolayer MoS₂, MoSe₂, WS₂, and WSe₂: spectroscopic ellipsometry and first-principles calculations. *Sci. Rep.* **10**, 15282 (2020).
51. Morozov, Y. V. & Kuno, M. Optical constants and dynamic conductivities of single layer MoS₂, MoSe₂, and WSe₂. *Appl. Phys. Lett.* **107**, 083103 (2015).
52. Jung, G.-H., Yoo, S. & Park, Q.-H. Measuring the optical permittivity of two-dimensional materials without a priori knowledge of electronic transitions. *Nanophotonics* **8**, 263–270 (2018).

Acknowledgements

Author contributions
A.J.M. and J.P. conceived the main ideas of this work. A.J.M. and A.Y. built the VAR and designed the polymer stamps. C.P. and A.J.M. formulated the TSL patterning technique. A.Y., F.M., C.P. and J.-H.K. grew the MOCVD TMD materials used in this work. A.Y. and A.J.M. manufactured the presented vdW solids using the VAR. A.Y. and M.L. acquired and analysed the optical measurements. A.Y. wrote the code and analysed the results from the TMM optical calculations and performed the laser confocal scanning microscopy and Raman mapping measurements. A.R. collected the FIB cross-section and STEM data. S.H.S. carried out the SAED and DF-TEM analysis of the twisted 4 L WS₂ structure, and performed the multislice simulation of

Additional information

Supplementary information The online version contains supplementary material available at https://doi.org/10.1038/s41565-021-01061-5.

Correspondence and requests for materials should be addressed to Jiwoong Park.

Peer review information *Nature Nanotechnology* thanks Jeehwan Kim and Zhi-Bo Liu for their contribution to the peer review of this work.

Reprints and permissions information is available at www.nature.com/reprints.